Arabian Journal for Science and Engineering

COUNTRY	SUBJECT AREA AND CATEGORY	PUBLISHER	H-INDEX
Germany Universities and research institutions in Germany Media Ranking in Germany	Multidisciplinary Multidisciplinary		70

PUBLICATION TYPE	ISSN	COVERAGE	INFORMATION
Journals	21914281, 2193567X	1984, 1986, 1996-2023	Homepage How to publish in this journal ajse@kfupm.edu.sa

SCOPE

The Arabian Journal for Science and Engineering (AJSE) is a peer-reviewed journal owned by King Fahd University of Petroleum and Minerals and published by Springer. AJSE publishes twelve issues of rigorous and original contributions in the Science disciplines of Biological Sciences, Chemistry, Earth Sciences, and Physics, and in the Engineering disciplines of Chemical, Civil, Computer Science and Engineering, Electrical, Mechanical, Petroleum , and Systems Engineering. Manuscripts must be submitted in the English language and authors must ensure that the article has not been published or submitted for publication elsewhere in any format, and that there are no ethical concerns with the contents or data collection. The authors warrant that the information submitted is not redundant and respects general guidelines of ethics in publishing. All papers are evaluated by at least two international referees, who are known scholars in their fields.

Join the conversation about this journal

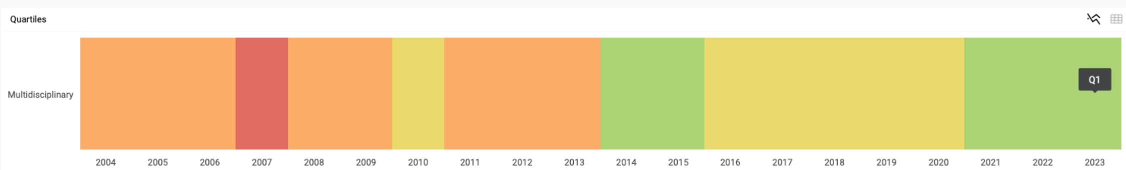

Arabian Journal for Science and Engineering
https://doi.org/10.1007/s13369-024-08805-0

RESEARCH ARTICLE-MECHANICAL ENGINEERING

Nanostructured Al–Ti–Fe–Mn–Ni High-Entropy Alloy by Mechanical Alloying: Synthesis and Characterization

Vivek Sharma[1] · Ashis Mallick[1] · Joydip Joardar[2] · Shakti Kumar[1] · S. V. Konovalov[3]

Received: 19 October 2023 / Accepted: 28 January 2024

Abstract

A multicomponent bulk nanostructured $Al_{20}Ti_{20}Fe_{20}Mn_{20}Ni_{20}$ high-entropy alloy (HEA) was prepared by the powder metallurgy method. The process involved mechanical alloying of the elemental powders of equal wt% followed by cold compaction and conventional sintering in an inert atmosphere at different temperatures. The structural evaluation and morphological studies of the milled powders were carried out by HRTEM and XRD analysis. The crystal size and d-spacing of the milled powder significantly reduced with the milling duration. The effects of sintering temperatures on the microstructure, wear resistance, and the hardness of $Al_{20}Ti_{20}Fe_{20}Mn_{20}Ni_{20}$ were investigated. The microstructural analysis showed that the prepared HEAs had a multiphase microstructure consisting of BCC and intermetallic compounds. As the sintering temperature grew, the microhardness and wear resistance increased, demonstrating that the properties of the current HEA were improved by using high sintering temperatures. The increase in density with sintering temperatures and the intermetallic phase contents acted as reinforcement might have enhanced the hardness of the HEA. The best hardness value and the least amount of wear were found in the sample sintered at 900 °C.

Keywords High-entropy alloy · Mechanical alloying · Powder metallurgy · Microstructure · Mechanical and wear properties

1 Introduction

In the past, traditional alloy systems, such as iron, copper, aluminum, and nickel-based alloys, were developed using one major element, and the concentration of one element was generally higher than that of the other minor alloying elements [1]. However, the new concept of alloy design and manufacture is different from the previous one and provides innumerable compositional variations for synthesizing novel materials [2]. This class of materials is known as high-entropy alloys (HEAs). High-entropy alloys are a new class of multicomponent alloys and are designed using a different approach to alloy design based on entropy configuration. These alloys contain minimum five elements, with the concentration of each element ranging from 5 to 35%. They are fabricated after considering the global minimum energy of formation of a solid solution by thermodynamic equilibrium, $\Delta G_{\text{mix}} = \Delta H_{\text{mix}} - T\Delta S_{\text{mix}}$. In this equation, ΔG_{mix} denotes Gibbs-free energy, ΔH_{mix} denotes the mixing enthalpy, ΔS_{mix} denotes the entropy mixing, and T denotes absolute temperature. Because of the high entropy of mixing, high-entropy alloys usually form simple BCC or FCC solid solution phases, amorphous structures, or even nanostructures instead of forming intermetallic compounds [3].

Four core effects, such as thermodynamic high-entropy, sluggish diffusion, structural lattice distortion, and cocktail effect have an impact on the resulting microstructure and mechanical properties of HEAs. The role of the core effects are as follows: (i) The high mixing entropy ΔS_{mix} of HEA solid solutions has a dominant effect on phase Gibbs energy ΔG_{mix}. As the mixing entropy of the system increases, the Gibbs-free energy decreases to its global minimum and stabilizes the solid solutions. (ii) The HEA lattices are severely

✉ Ashis Mallick
mal123_us@yahoo.com; mallick@iitism.a.in

1 Department of Mechanical Engineering, Indian Institute of Technology (ISM) Dhanbad, Dhanbad 826 004, India

2 International Advanced Research Centre for Powder Metallurgy and New Materials (ARCI), Hyderabad 500 005, India

3 Siberian State Industrial University, 42 Kirova Str., Novokuznetsk, Kemerovo Region – Kuzbass, Russian Federation 654007

Published online: 05 March 2024

strained due to the size mismatch between the alloying elements. This, in turn, has various impacts on the chemical and physio-mechanical properties of HEAs. (iii) HEAs show a sluggish diffusion effect since atomic diffusion is more challenging through solid solutions having high concentrations of many elements, mostly as a result of changes in the bonding environment caused by their lattices. (iv) The microstructural complexity of HEAs gives rise to the 'cocktail effect' in which the interactions between different elements produce unusual behaviors, resulting in an average alloy property. The role of these four core effects has been shown in several studies on HEAs by various research groups [4, 5]. The high-entropy alloy (HEA) $Fe_{20}Cr_{20}Mn_{20}Ni_{20}Co_{20}$, has a single-phase face-centered cubic (FCC) lattice structure and is one of the most-studied and well-understood HEA [6]. The HEA $Fe_{20}Cr_{20}Mn_{20}Ni_{20}Co_{20}$ has high ductility [7, 8]. Huang et al. [9] produced a single-phase Co-free equiatomic FCC structured CuFeMnNi HEA in which several thermo-mechanical processes were used to adjust the ductility and strength. Various research has found that single-phase HEAs usually exhibit lower hardness, strength, and wear resistance [2]. While the AlCoCrFeNi-based HEAs showed a mixture of FCC and BCC phases [10, 11]. These alloys have drawn much interest due to their potential corrosion resistance and mechanical properties.

Several methods have been employed to improve the chemical, physical, and mechanical properties of HEAs [12]. The atomic composition and crystalline size of HEAs can be tuned to get the desired properties. Studies on abrasion resistance, wear resistance, oxidation resistance, corrosion resistance, and high-temperature resistance have tremendously increased in the field of metal materials research [13, 14]. By varying the composition, materials with better physical and mechanical properties can be produced. Waseem et al. [15] found that changing the composition of tungsten in W_xTaTiVCr HEA from $x = 90\%$ to $x = 42\%$ enhanced the microhardness and compression. The influence of materials and machining parameters on the wire electric discharge machining (WEDM) of particle-reinforced high-entropy alloy composites was studied by Karthik et al. [16].

A solid-state method based on powder metallurgy technique, where high/medium energy ball milling or mechanical alloying (MA) is followed by consolidation processes and conventional sintering, enables industrial mass production of nanocrystalline materials with enhanced mechanical, physical, chemical, and corrosion properties [17–19]. Ball milling is a technique that might induce either the mechanical activation of the raw powder mixture or the complete transformation of metal powder reactants into alloys at room temperature [20, 21]. This process of complete transformation into new alloys is usually referred to as mechanical alloying (MA), mechanical synthesis, or mechanochemical synthesis. Most studies on the synthesis of HEAs are based on powder metallurgy that performs MA with a complete chemical reaction at room temperature [22]. Rogal et al. [23] employed mechanical alloying to prepare $Al_{25}Co_{25}Cr_{25}Fe_{25}$ alloy using powder metallurgy technique. The synthesized alloy exhibited high compression strength of 3920 MPa with an increased yield strength of 3500 MPa at a small strain of 0.7%.

In this study, we developed a lightweight, strong, and wear-resistant $Al_{20}Ti_{20}Fe_{20}Mn_{20}Ni_{20}$ high-entropy alloy composite using the powder metallurgy technique. In order to synthesis low-density HEA, Al (~ 2.7 g/cm^3) and Ti (~ 2.7 g/cm^3) were used in place of the elements Cr (~ 7.15 g/cm^3) and Co (~ 8.90 g/cm^3). The microstructure of the mechanically alloyed powders and the corresponding bulk sintered samples were studied. The BCC solid solution phase served as the matrix, and the intermetallic phase served as reinforcement in the microstructure of the alloy composite. The wear properties of the HEA samples were studied by the universal tribotester machine, while the hardness values were estimated by conducting the micro-indentation test. The loading and unloading behaviors of micro-indention were also investigated. Based on the findings of this study, we envisage that HEAs with appropriate microstructure could be used in various structural applications requiring high wear resistance, high strength, and high-temperature capabilities.

2 Materials and Methods

The $Al_{20}Ti_{20}Fe_{20}Mn_{20}Ni_{20}$ lightweight nanostructured high-entropy alloys were manufactured using the powder metallurgy technique. Aluminum, titanium, iron, manganese, and nickel powder were used as raw materials with particle sizes in the range of 40–70 µm. Aluminum and titanium with 99.9% purity were purchased from Alfa Aesar (Haverhill, MA, USA), and iron, manganese, and nickel with 99.5% purity level were purchased from Sisco Research Laboratories, India. A high-energy planetary ball milling machine was used for pre-mixing and mechanical alloying. Stainless-steel vials and stainless-steel SS316 balls were used as milling media. During the milling of the elemental powders, the ball to powder ratio was taken as 10:1. Stearic acid was used to prevent the excessive cold welding of powders during mechanical alloying. For mechanical alloying, the machine was operated at 250 rpm for 28 h following the sequence of 10 min clockwise rotation, 10 min anticlockwise rotation, and 10 min standby for homogeneous mixing and preventing excessive heat generation. After 28 h of ball milling, the powder was dried for 5 h at 50 °C in a vacuum oven. The dried powder (~ 2 g) was cold compacted in a cylindrical die at 500 MPa to produce 8 mm in diameter and 8 mm in height cylindrical samples. The cold compacted samples were sintered for 2 h in a tabular furnace with an argon

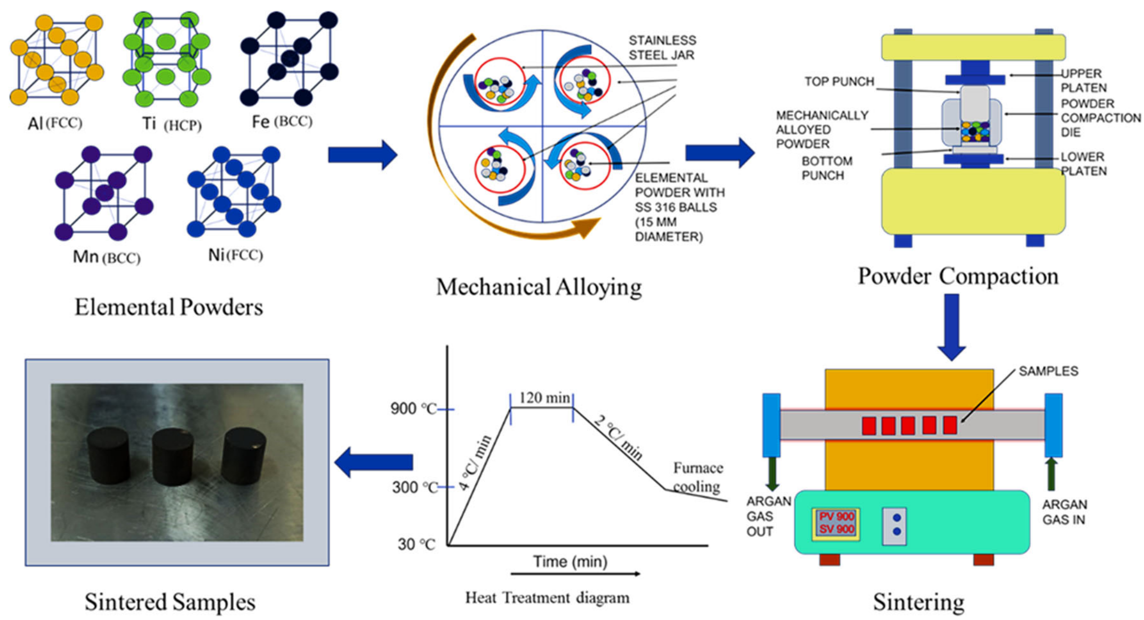

Fig. 1 Schematic diagram representing the process to manufacture the lightweight high-entropy alloy (HEA)

environment at temperatures of 700, 800, and 900 °C. The densities of bulk green and sintered samples were measured using the Archimedes principle. The sintered samples were polished using 500, 600, 1000, 1500, and 2000 grit papers, followed by a diamond paste (0.5 µm) for investigations. In order to present consistent results, three samples in each sintered temperature were considered for every investigation. The schematic diagram of the entire process for manufacturing bulk nanostructured $Al_{20}Ti_{20}Fe_{20}Mn_{20}Ni_{20}$ HAEs from the elemental powders is presented in Fig. 1.

The microstructural characterization of the powder and sintered samples was accomplished by X-ray diffraction analysis (XRD) and electron microscopy. The characterization included an examination of the phase detection of the HEA samples, elemental distribution of the particles, porosity, and nanostructure formation. The crystal structure, constituent phases, and the changes in the texture of the ball-milled powder and the sintered samples of HEAs were examined by conducting the XRD (Rigaku-Smartlab, Tokyo, Japan) analysis. The machine was operated at a 2θ scanning rate of 4°/min using Cu–Kα radiation. The phase morphology, diffraction pattern, crystallographic planes, composition, and the EDS mapping spectrum of the milled powder and sintered samples were determined using FESEM (Supra 55, Carl Zeiss, Germany) and HRTEM (Talos F200X G2, Thermo-Scientific, USA) analysis.

Micro-indentation tests were performed on the sintered samples using a depth-sensing, fully computerized MTR3/50–50/NI microhardness tester (Microtest S.A., Spain). The indentation load was applied using Vickers pyramidal indenter (phase angle 136°) following ASTM standard E384. The machine was operated for a dwell time of 30 s with a maximum load of 5 N at a constant loading and unloading rate of 0.1 N/s. A 4 × 4 indentation matrix was created on the HEA samples (8 mm diameter) with 0.5 mm spacing between each indent, and for the study, the average value acquired from the indentation matrix was taken into consideration. Before indentation, the surfaces of each sample were flattened and mirror-polished. For each indentation cycle, the curves for force versus displacement were generated, and the elastic modulus and hardness were calculated from the unloading curves. The Vickers microhardness (H_{v}) and Martens hardness (HM) were estimated from the force-indentation depth curves based on the following relationship:

$$H_{\mathrm{V}} = \frac{0.371P}{h_V^2}\ \mathrm{MPa} \tag{1}$$

$$\mathrm{HM} = \frac{P}{26.43h_{\mathrm{m}}^2}\ \mathrm{MPa} \tag{2}$$

Here, P denotes the maximum applied load through the indenter, h_{m} denotes the maximum indentation depth under the working load, and h_v denotes the indentation depth measured after unloading. The percentage of elastic recovery after indentation was measured using the following equation:

$$\%\ \text{elastic recovery} = \frac{H_{\mathrm{V}} - \mathrm{HM}}{H_{\mathrm{V}}} \times 100 \tag{3}$$

The dry sliding reciprocating wear tests of bulk HEA samples were conducted using a Universal Tribometer (Rtec Instruments USA-MFT500) machine. A stainless-steel ball (5 mm diameter) was used to slide back and forth over the

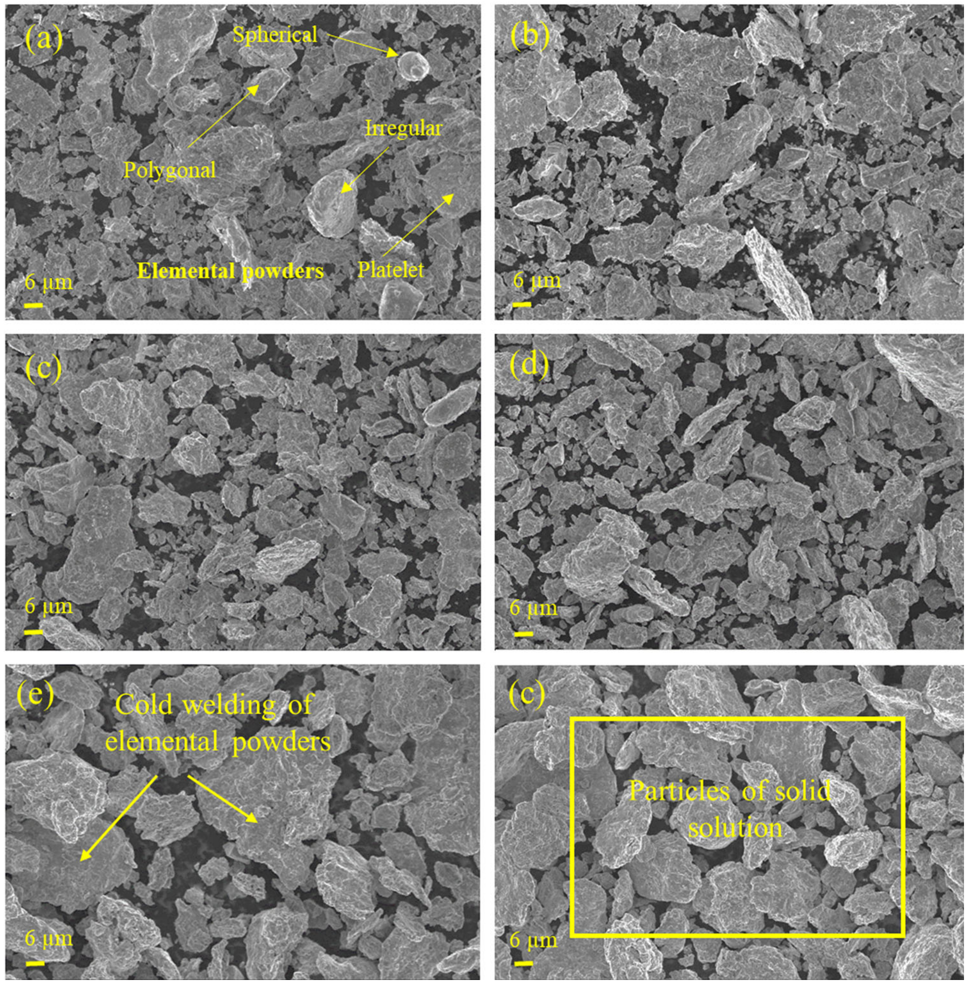

Fig. 2 The FESEM images of the ball- milled powder of $Al_{20}Ti_{20}Fe_{20}Mn_{20}Ni_{20}$ after **a** 4 h, **b** 8 h, **c** 12 h, **d** 16 h, **e** 20 h, and **f** 28 h

flat and polished surface of the samples. The test was performed at a constant normal load of 20 N for 10 min through 5 mm stroke length distance at a frequency of 3 Hz. To maintain the consistency of the results, at least three sliding tests were conducted for each sample. The wear depth and width of the flat molded samples were measured using a 3D optical profilometer (NewView 9000 ZYGO, USA). The morphological characteristics of the worn surfaces were investigated by performing the FESEM analysis.

3 Results and Discussion

The effect of the milling hours on the variation of morphologies of the mechanically alloyed (MA) powders is shown in Fig. 2.

The morphology of MA powders, as shown in Fig. 2a–d exhibited a mixture of different elemental particles having different shapes and sizes. At the initial stage of milling, the fracturing mechanism dominates to produce fine powder particles. With the increase in the milling time from 4 to 16 h (Fig. 2a–d), the average granular size of the milled powder gradually decreased to 10 µm (average diameter) from the primitive powder (maximum size: 70 µm diameter). In contrast, with a further increase in milling duration, the granular size of the milled powder increased due to an increase in mass concentration (Fig. 2e–g) by the cold welding of neighboring particles and high-configurational entropy. The MA powders milled for 28 h produced mostly equiaxed particles (Fig. 2g) through continuous cold welding and fracturing, which suggested that the present HEA met the steady-state condition. The average granular size after 28 h of milling was estimated to be 13 µm. The TEM images of the 28 h milled powder are illustrated in Fig. 3. The selected area diffraction (SAD) pattern of the milled powder (Fig. 3a) revealed the presence of multiple phases and the formation of nanograins. The reduction of crystalline size with the milling duration promotes the sold solution. Thus, the conversion of elemental powder into a solid solution is facilitated by the process of cold welding and fracturing, which is induced by high-energy ball milling. The findings in Fig. 3b confirmed the formation of crystalline in the MA powder milled for 28 h.

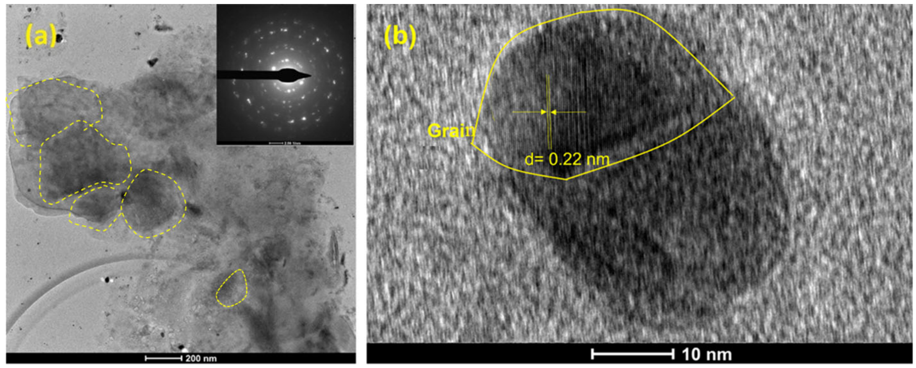

Fig. 3 **a** The dark field TEM image of the 28 h ball-milled powder and the diffraction pattern; **b** The crystalline planes

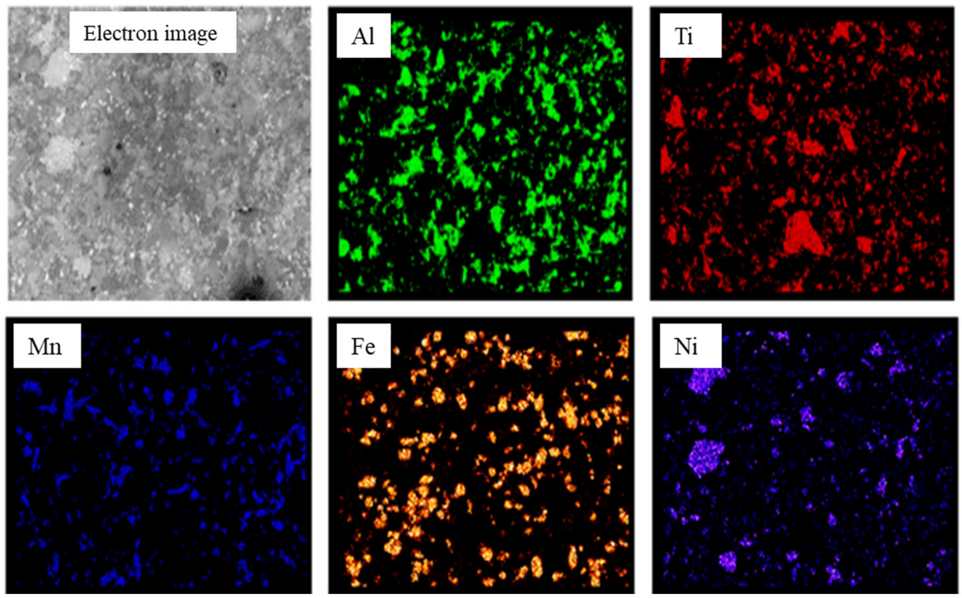

Fig. 4 The surface morphology of the $Al_{20}Ti_{20}Fe_{20}Mn_{20}Ni_{20}$ HEA composite sintered at 900 °C and the corresponding EDS maps of the typical regions

Figure 4 depicts the SEM micrograph and the corresponding EDS area mapping of the compacted cylindrical billet of the $Al_{20}Ti_{20}Fe_{20}Mn_{20}Ni_{20}$ HEA that was sintered at 900 °C for 2 h. Before compaction, the powders were mechanically alloyed for 28 h. The local phase composition of the sintered samples was measured by performing EDS area mapping and based on the EDS spectra at different points. The surface morphology of the HEA indicated the formation of a high-entropy BCC solid solution along with well-distributed intermetallic phases (Fig. 4a). The corresponding EDS area mapping (Fig. 4b–f) further confirmed that all base elements were distributed in bulk sintered HEA sample. However, a slightly uneven distribution of the elements was observed on the EDS map, possibly an uneven capture of particles occurred due to disorganized energy distribution in the milling process. The presence of all the elements in in the EDS map suggested that the alloying was achieved by the continuous welding and fracture of powdered particles during high-energy ball milling and the sintering at high temperature. This phenomenon was further investigated by the EDS spectrum at different points of the bulk sample.

Table 1 shows the elemental percentage (atomic % and wt%) at the different points of the HEA sample sintered at 900 °C. The EDS spectrum 1 indicated the formation of a solid solution comprising a phase with all elements. In contrast, spectrum 2 and 3 detected an Al–Ti-rich intermetallic phase, while spectra 4 corresponded to a pore surrounding with a major Al phase. The densities of the bulk green sample and the extruded samples of $Al_{20}Ti_{20}Fe_{20}Mn_{20}Ni_{20}$ HEA are presented in Table 2. The compaction of nanostructured powder at room temperature is a great challenge due to large strain hardening and severe plastic deformation. Additional surface energy is required to enhance the packing of the powder particles. As a result, the green compacted sample showed poor density. In contrast, the consolidated powder particles were fused during sintering at high temperatures. It can be seen that the density of the bulk sample was increased with the sintering temperature, which revealed that the formation of better crystalline growth occurred at higher sintering temperatures.

Table 1 The elemental distribution of $Al_{20}Ti_{20}Fe_{20}Mn_{20}Ni_{20}$ HEA sintered at 900 °C

FESEM image of the bulk $Al_{20}Ti_{20}Fe_{20}Mn_{20}Ni_{20}$ HEA	Spectra	wt % and atomic %	Element %				
			Al	Ti	Mn	Fe	Ni
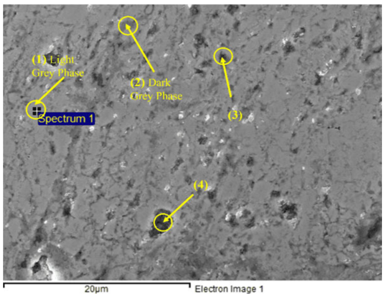	1	wt%	18.95	9.78	20.74	26.04	24.50
		Atomic %	32.40	9.42	17.41	21.51	19.25
	2	wt%	28.09	35.41	18.70	11.18	6.61
		Atomic %	42.78	30.38	13.99	8.22	4.63
	3	wt%	28.66	21.55	18.58	17.89	13.32
		Atomic %	44.31	18.77	14.11	13.36	9.46
	4	wt%	56.69	13.63	13.47	9.71	6.50
		Atomic %	72.07	9.76	8.41	8.97	3.80

Table 2 The effect of sintering on the density of the bulk $Al_{20}Ti_{20}Fe_{20}Mn_{20}Ni_{20}$ HEAs

Green density of bulk sample (g / cc)	Density of sintered sample (g / cc)		
	HEA 700 °C	HEA 800 °C	HEA 900 °C
3.94	4.03	4.120	4.344

The XRD line profile of the $Al_{20}Ti_{20}Fe_{20}Mn_{20}Ni_{20}$ HEA powders after MA and the bulk sintered samples are presented in Fig. 5. The phases were identified using Crystal Impact Match software (version 3.8). Figure 5a shows the influence of milling duration on the $Al_{20}Ti_{20}Fe_{20}Mn_{20}Ni_{20}$ powder blend. Broadening of the peaks is evident from the magnified view of selected peaks in Fig. 5b. Marginal peak shift is also observed, indicating some interdiffusion of the elements under mechanical deformation induced processing. However, no intermetallic phase could be detected even at the end of 28 h of milling. The final ball-milled powder contained all the elemental powders in the starting blend albeit with refined crystallite size, as reflected by the peak broadening. It may be noted that past reports on MA of many of the binary and ternary elemental systems demonstrated the extension in solid solubility or extension of phase field instead of intermetallic phase formation instead of ordered intermetallic phase formation. For example, the widely studied Fe–Al system [24] showed the formation of a BCC Fe(Al) solid solution over an extended phase field of Fe-50at%Al composition on MA for 600 h. Figure 5c–e shows the phase analysis of the consolidated samples sintered at 700, 800, and 900 °C. The orthorhombic Fe_4Al_{11} (Space group: C^2/m) is observed in samples sintered at 700 and 800 °C, which disappears at higher temperature sintering at 900 °C. It may be noted that Fe_2Al_5 (that is, Fe_4Al_{10}) is known to exist with a composition varying between Fe_4Al_9 and Fe_4Al_{11} [25, 26]. Its formation from Fe-40 at% Al powder blend has been observed above 560 °C in dilatometric studies [27]. As demonstrated in previous studies, the formation of Fe_2Al_5 phase is observed ahead of other thermodynamically more stable phases in the Fe–Al system as favored by kinetic factors [28, 29]. However, on heating to a higher temperature (e.g., 1000 °C), Fe_2Al_5 reacts with Fe and transforms to Fe–Al (ordered BCC phase (CsCl type) with space group: Pm-3m) [28]. In the present work, Fe_4Al_{11} (Fe_2Al_5) disappears in the sample sintered at 900 °C and shows BCC-type phase like $Fe_{0.3}Ni_{0.32}Al_{0.38}$ (Space group: Im-3m). The other prominent phases in the sintered samples are AC_2X- or BC_2X-type phases with FCC (Space group: Fm-3m)-based structure where A, B, and C are transition elements with A = Ti (Group IVB element), B = Mn (Group VIB element), C = Fe or Ni (Group VIII elements), and X = Al. These phases are Heusler alloy-type phases, some of which are expected to have excellent mechanical properties [30]. In addition to these phases, some fractions of other BCC and hexagonal phases are also evident from the phase analysis shown in Fig. 5c–e.

Table 3 shows the list of all possible major, minor, and trace phases in the sintered samples (Fig. 5c–e). The presence of high intensity peak at a 2θ of 30.8° at the lower sintering temperatures of 700 and 800 °C possibly indicate the presence of higher fraction of $TiNi_2Al$ and Fe–Al-based phases. The presence of such a multiphase structure with Heusler-type matrix (major) phases (cubic: Fm-3m structure) is expected to contribute significantly to the mechanical properties of the sintered composites.

To determine the mechanical strength of the synthesized bulk HEA, micro-indentations were made on the polished surface of the HEAs. The representative loading and unloading curves of the micro-indentations are presented in Fig. 6. The loading and unloading curves of the HEA samples sintered at 900 °C were considerably steeper than the sample sintered at 800 °C and 700 °C. The indentation depth against

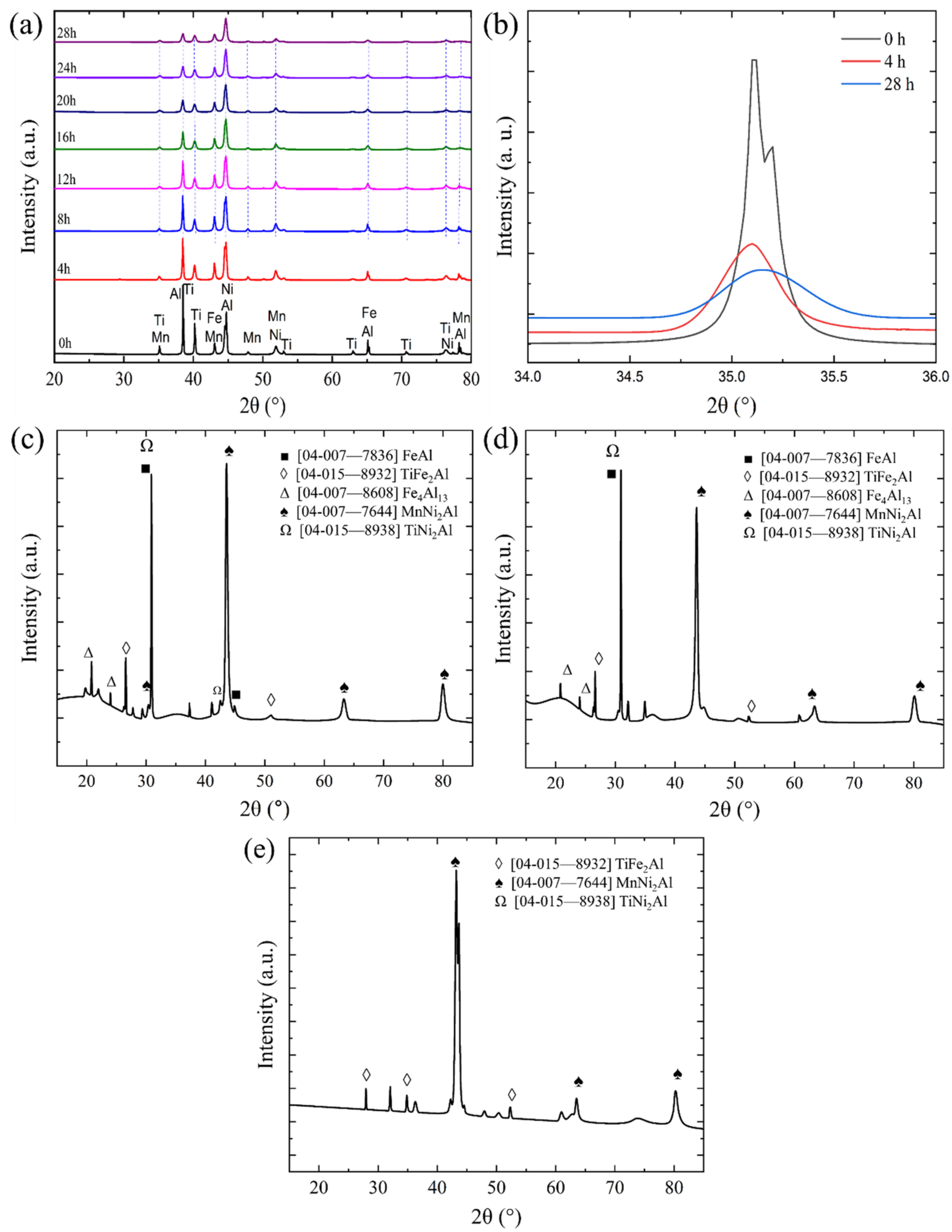

Fig. 5 **a** The XRD pattern of the 0–28 h ball-milled powder and **b** Peak shift during the milling of milled powder, **c** HEA sintered at 700 °C, **d** HEA sintered at 800 °C, **e** HEA sintered at 900 °C

the maximum indentation force of 5 N was notably higher in the sample sintered at 700 °C, followed by indentation depth at 800 °C and 900 °C, respectively. These results suggested that the bulk HEA sample was stronger when it was sintered at 900 °C, probably due to the higher fraction of Heusler-type phase formation as matrix phase and the presence of other multiphase grains. Almost similar patterns of loading and unloading curves were observed for all samples. However, different indentation depths before and after unloading were observed. The plastic deformation and elastic–plastic deformation of the HEA samples were measured from the force-indentation depth curves by calculating the conventional Vickers microhardness value (H_V) and Martens hardness value (HM) based on the relationship as mentioned in Eqs. (1) and (2).

Vickers microhardness value (H_V), Martens hardness value (HM), and the percentage of elastic recovery of the HEA samples sintered at three different temperatures are presented in Table 4. The values in the table were estimated as the mean of the 10 best values of the indentation matrix. With an increase in sintering temperature, the H_V and HM values increased substantially. The H_V ~ 9.92 GPa and HM ~ 3.51 were estimated for the sample sintered at 900 °C and were about 1.43 and 1.26 times higher than that of the sample sintered at 700 °C and 1.32 and 1.08 times higher than that of the sample sintered at 800 °C. These results suggested that

Table 3 The possible phases in the samples sintered at different temperatures, as ascertained from the XRD qualitative analysis. The space group of the phases are also indicated

Sintering temperature (°C)	Major phase(s)	Minor phase(s)	Trace phase(s)
700	$TiNi_2Al$ (Fm-3m) $TiFe_2Al$ (Fm-3m) $MnNi_2Al$ (Fm-3m) Fe_2AlTi (Fm-3m) $Mn_{0.5}Ni_{0.5}Al$ (Pm-3m)	Fe–Al (Pm-3m) $Fe_{0.6}Al_{0.4}$ (Im-3m) Fe_4Al_{13} (C2/m) $Ti_{0.17}Mn_{0.83}$ (R-3) $TiMn_2$ (P63/mmc) $TiFe_2$ (P63/mmc)	MnO_2 (P42/mnm) Fe_2O_3 (R-3c) Ti–Ni (P21/m) Ti_3Al (P63/mmc) $Mn_{0.72}Al_{0.28}$ (R-3m)
800	$TiNi_2Al$ (Fm-3m) $TiFe_2Al$ (Fm-3m) $MnNi_2Al$ (Fm-3m) Fe_2AlTi (Fm-3m) $Mn_{0.5}Ni_{0.5}Al$ (Pm-3m)	Fe–Al (Pm-3m) Fe_4Al_{13} (C2/m) $Ti_{0.17}Mn_{0.83}$ (R-3) $TiMn_2$ (P63/mmc) $TiFe_2$ (P63/mmc)	MnO_2 (P42/mnm) Fe_2O_3 (R-3c) Ti–Ni (P21/m) Ti_3Al (P63/mmc) $Mn_{0.72}Al_{0.28}$ (R-3m)
900	$TiFe_2Al$ (Fm-3m) $MnNi_2Al$ (Fm-3m) Fe_2AlTi (Fm-3m) $Fe_{0.453}Ni_{0.449}Al_{0.098}$ (Fm-3m) $Ti_{0.21}FeAl_{0.79}$ (Pm-3m) $Ti_{0.4}Ni_3Al_{0.6}$ (Pm-3m)	$TiNi_2Al$ (Fm-3m) $Ti_{0.2}Fe_{0.8}$ (Im-3m) Ti–Fe (Pm-3m)	Ti–Fe–Al (P63/mmc) $TiFe_2$ (P63/mmc)

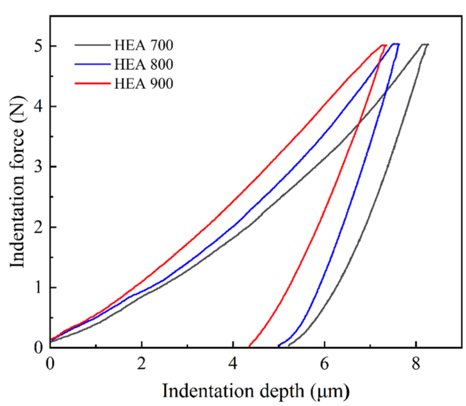

Fig. 6 The variation of the loading and unloading curves of the micro-indentation test on the HEA samples sintered at 700 °C, 800 °C, and 900 °C

Table 4 The microhardness values of $Al_{20}Ti_{20}Fe_{20}Mn_{20}Ni_{20}$ HEAs sintered at different temperatures

Material	HEA 700 °C	HEA 800 °C	HEA 900 °C
H_v (GPa)	6.91	7.492	9.92
HM (GPa)	2.78	3.253	3.51
% of elastic recovery	59.77	56.58	64.61

Table 5 The average coefficients of friction for the $Al_{20}Ti_{20}Fe_{20}Mn_{20}Ni_{20}$ HEAs sintered at different temperatures

Materials	HEA 700 °C	HEA 800 °C	HEA 900 °C
Ave. COF	0.34	0.36	0.53

the density of the HEA sample increased with the increase in the sintering temperature. This phenomenon can be elucidated by the densification of the body, which facilitates the partial elimination of porosity when exposed to elevated temperatures. In fact, the thermal energy induces a force with the increase in sintering temperature that causes the grain boundaries to expand and reduce pore volume, resulting in an increase in material density. The percentage of elastic recovery was considerably higher in the HEA sample sintered at 900 °C. An increase in hardness along with higher elastic recovery revealed that the $Al_{20}Ti_{20}Fe_{20}Mn_{20}Ni_{20}$ HEA had better structural properties when it was sintered at 900 °C.

The coefficient of friction (COF) of the bulk sample of $Al_{20}Ti_{20}Fe_{20}Mn_{20}Ni_{20}$ HEAs were determined by conducting the wear test under dry sliding conditions. The coefficient of friction depended on the normal load (N) applied to the spherical ball (5 mm), and the corresponding force (F_s) required to slide the ball on the surface of the sample. Table 5 represents the values COF of the $Al_{20}Ti_{20}Fe_{20}Mn_{20}Ni_{20}$ HEAs sintered at different temperatures. It can be observed that the sample sintered at 900 °C had considerably higher

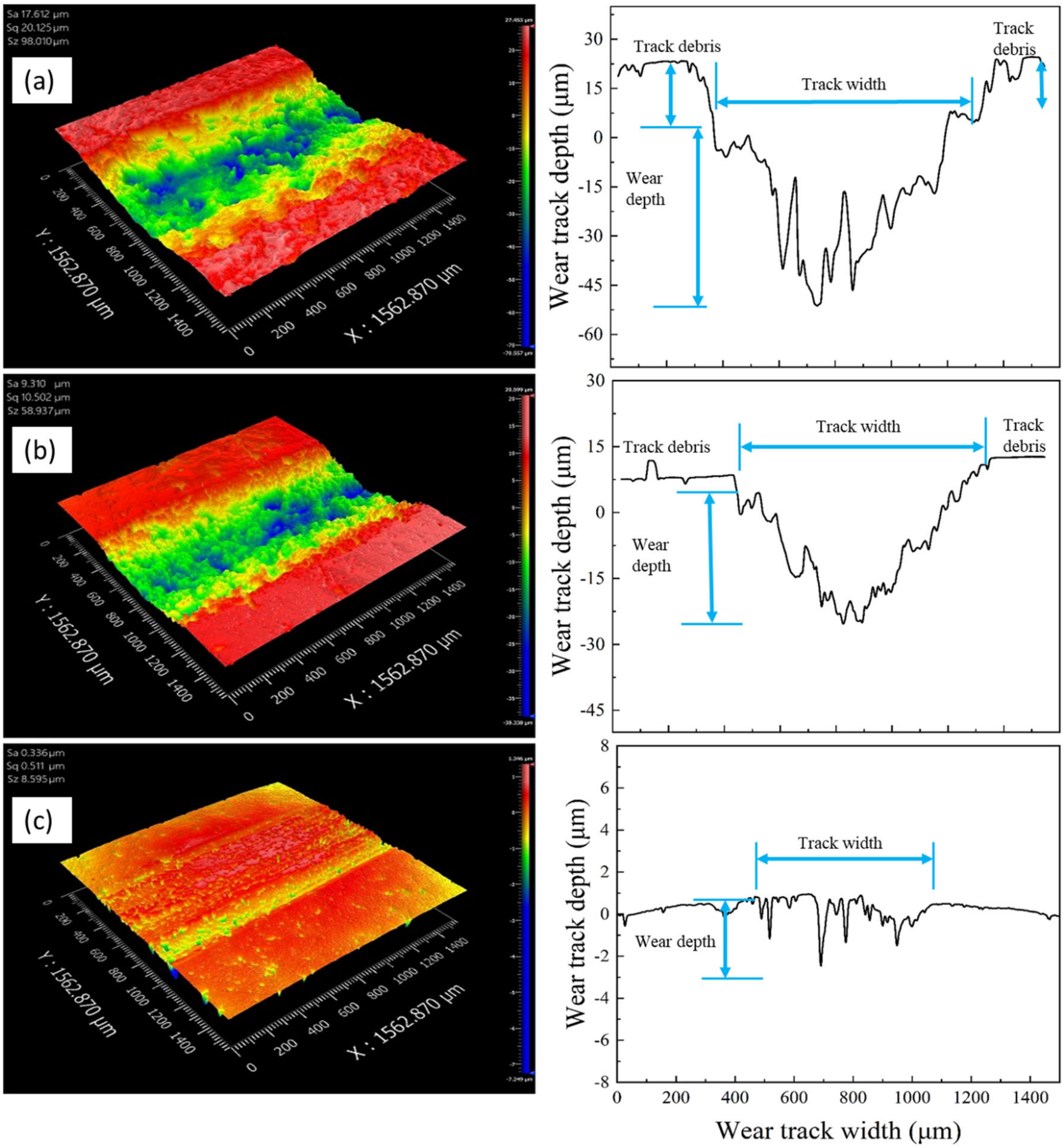

Fig. 7 The 3D optical image of the profile of the worn tracks of the HEA samples sintered at **a** 700 °C, **b** 800 °C, and **c** 900 °C under a normal load of 20 N on the surface

average COF (= F_s/N) under normal load 20 N than that of the samples sintered at 800 °C and 700 °C. This might be due to a higher rubbing force required for scraping the hard particles while sliding over the surface of the sample sintered at 900 °C.

The 3D optical images of the wear track morphology and the corresponding wear width and depth under 20 N normal load are shown in Fig. 7. Material peelings and grooves were present in all samples. The maximum wear depth obtained from the pitting surfaces was about 50 µm, 30 µm, and 3 µm in the samples sintered at 700 °C, 800 °C, and 900 °C, respectively. These results suggested that the samples sintered at 700 °C and 800 °C were softer than those sintered at 900 °C. Despite the lowest depth of the wear track and the corresponding lowest volume of the wear of the samples sintered at 900 °C, a large sliding force (F_S) was required to scrape the hard microparticles, which was predominantly responsible for the higher COF in the sample sintered at 900 °C. Similar results for the coefficient of friction under dry sliding conditions were reported in other studies [31, 32].

The optical micrograph illustrated in Fig. 8a further aided to perform the surface characterization of the bulk HEA samples. A similar trend, as discussed before, was observed for the worn surfaces sintered at different temperatures. The

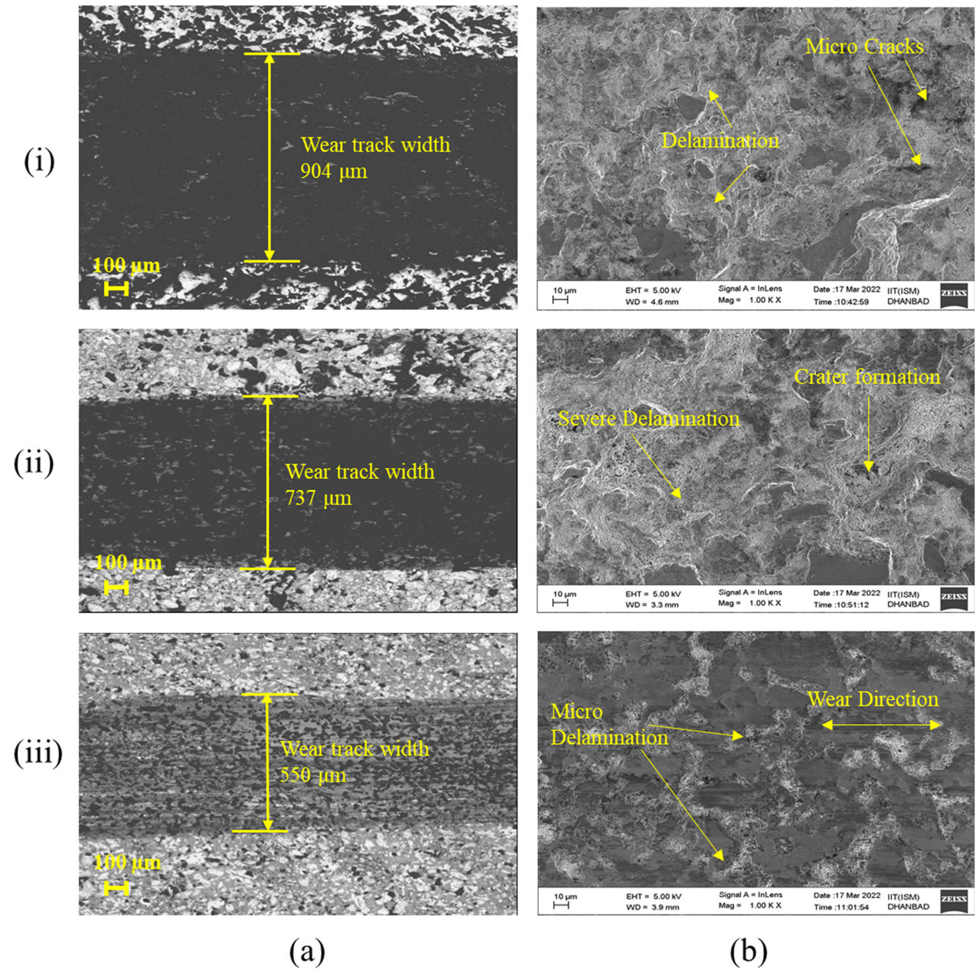

Fig. 8 The optical images of **a** the wear tracks and the corresponding **b** FESEM images of the micrographs of worn-out surfaces for the samples sintered at (i) 700 °C, (ii) 800 °C, (iii), and 900 °C

corresponding FESEM micrographs (Fig. 8b) of the worn surfaces predicted the insight of the wear mechanism. Oxidation of the wear track was also observed, which might be the result of heat generation on the surfaces due to rubbing during the wear test. Relatively milder abrasive and adhesive wear with a lesser quantity of material removed from the sample sintered at 900 °C (Fig. 8b) suggested that $Al_{20}Ti_{20}Fe_{20}Mn_{20}Ni_{20}$ HEA had good wear resistance at high sintering temperatures.

4 Conclusions

The $Al_{20}Ti_{20}Fe_{20}Mn_{20}Ni_{20}$ HEAs were successfully prepared by mechanical alloying followed by cold compaction and conventional sintering in an inert atmosphere. The BCC solid phase mainly occurred in the milled powder and the bulk sintered samples. The crystal size of the milled powder decreased to nanosize after milling for 28 h. The findings of this study are summarized as follows:

(i) A high-strength BCC high-entropy alloy composite of $Al_{20}Ti_{20}Fe_{20}Mn_{20}Ni_{20}$ was produced using the powder metallurgy technique.

(ii) When the sintering temperature was raised from 700 to 900 °C, the bulk $Al_{20}Ti_{20}Fe_{20}Mn_{20}Ni_{20}$ HEA showed less severe wear, which indicated that higher temperatures resulted in a better solid solution as the matrix.

(iii) The wear mechanisms of the $Al_{20}Ti_{20}Fe_{20}Mn_{20}Ni_{20}$ HEAs included a mixture of adhesive wear and three-body abrasive wear caused by the trapped wear debris on the wear track. Severe plastic and shear deformation were also associated with the wear mechanism. The three-body abrasive mechanism was less dominant in the samples sintered at 900 °C.

(iv) The $Al_{20}Ti_{20}Fe_{20}Mn_{20}Ni_{20}$ HEA sintered at 900 °C had the highest Vickers and Martens microhardness values of about 9.92 GPa and 3.51, respectively. The elastic recovery strongly influenced the results of the hardness test.

(v) The coefficient of friction was measured by determining the ratio of scrape force to normal force and was the highest in the $Al_{20}Ti_{20}Fe_{20}Mn_{20}Ni_{20}$ HEA sample sintered at 900 °C.

(vi) The mechanical and tribological properties of the bulk $Al_{20}Ti_{20}Fe_{20}Mn_{20}Ni_{20}$ HEA depended on the grain size, sintering temperature, and the existence of intermetallic phases in the HEA matrix.

Acknowledgements The authors wish to acknowledge the financial support for this work given by Science and Engineering Research Board (SERB), Department of Science & Technology, Govt. of India, vide Sanction order No. EEQ/2018/001160 dated 18.03.2019.

Author Contributions Vivek Sharma contributed to experimental investigations, methodology, formal analysis, and writing the original draft of the manuscript. Ashis Mallick was involved in conceptualization, methodology, review and re-writing the manuscript, and supervise the work. Joydip Joardar contributed to rewrite the XRD analysis and provide a few critical technical notes to improve the article. Shakti Kumar—assist with the execution of a few experiments and their analysis. S. V. Konovalov—examine the article and provide suggestions along with technical key points for improving the manuscript.

Data Availability Data will be made available on request.

Declarations

Conflict of interest The authors are here, declaring no conflict of interest in this work for publication.

Ethical Approval Not applicable.

References

1. Chen, Q.S.; Lu, Y.P.; Yong, D.O.; Wang, T.M.; Li, T.J.: Effect of minor B addition on microstructure and properties of AlCoCrFeNi multi-compenent alloy. Trans. Nonferr. Met. Soc. China **25**(9), 2958–2964 (2015)
2. Gludovatz, B.; Hohenwarter, A.; Catoor, D.; Chang, E.H.; George, E.P.; Ritchie, R.O.: A fracture-resistant high-entropy alloy for cryogenic applications. Science **345**(6201), 1153–1158 (2014)
3. Torralba, J.M.; Alvaredo, P.; García-Junceda, A.: High-entropy alloys fabricated via powder metallurgy. A critical review. Powder Metall. **62**(2), 84–114 (2019)
4. Nutor, R.K.; Cao, Q.; Wang, X.; Zhang, D.; Fang, Y.; Zhang, Y.; Jiang, J.Z.: Phase selection, lattice distortions, and mechanical properties in high-entropy alloys. Adv. Eng. Mater. **22**(11), 2000466 (2020)
5. Wang, X.; Guo, W.; Fu, Y.: High-entropy alloys: emerging materials for advanced functional applications. J. Mater. Chem. A **9**(2), 663–701 (2021)
6. Cantor, B.; Chang, I.T.; Knight, P.; Vincent, A.J.: Microstructural development in equiatomic multicomponent alloys. Mater. Sci. Eng. A **375**, 213–218 (2004)
7. Eißmann, N.; Klöden, B.; Weißgärber, T.; Kieback, B.: High-entropy alloy CoCrFeMnNi produced by powder metallurgy. Powder Metall. **60**(3), 184–197 (2017)
8. Abbasi, E.; Dehghani, K.: Phase prediction and microstructure of centrifugally cast non-equiatomic Co–Cr–Fe–Mn–Ni (Nb, C) high entropy alloys. J. Alloy. Compd. **783**, 292–299 (2019)
9. Huang, X.; Miao, J.; Li, S.; Taylor, C.D.; Luo, A.A.: Co-free CuFeMnNi high-entropy alloy with tunable tensile properties by thermomechanical processing. J. Mater. Sci. **56**, 7670–7680 (2021)
10. Aizenshtein, M.; Strumza, E.; Brosh, E.; Hayun, S.: Precipitation kinetics, microstructure, and equilibrium state of A2 and B2 phases in multicomponent $Al_{2.75}$CoCrFeNi alloy. J. Mater. Sci. **55**, 7016–7028 (2020)
11. Dong, Y.; Lu, Y.: Microstructure and mechanical properties of $CoCrFeNi_2Al_{1-x}W_x$ high entropy alloys. Arab. J. Sci. Eng. **44**, 803–808 (2019)
12. Jun, X.U.; Cao, C.M.; Ping, G.U.; Peng, L.M.: Microstructures, tensile properties and serrated flow of AlxCrMnFeCoNi high entropy alloys. Trans. Nonferr. Met. Soc. China **30**(3), 746–755 (2020)
13. Zhou, Z.; Cui, T.; Guo, H.; Lv, W.; Wang, J.; Peng, X.: Laser additively manufacturing of $Al_{0.5}CoCrFeNiTi_{0.5}$ high-entropy alloys with increased resistances to corrosion 3.5% NaCl and oxidation at 1000 °C. J. Mater. Sci. **58**, 10148–10165 (2023)
14. Zhang, T.; Xin, L.; Wu, F.; Zhao, R.; Xiang, J.; Chen, M.; Jiang, S.; Huang, Y.; Chen, S.: Microstructure and mechanical properties of FexCoCrNiMn high-entropy alloys. J. Mater. Sci. Technol. **35**(10), 2331–2335 (2019)
15. Waseem, O.A.; Ryu, H.J.: Powder metallurgy processing of a WxTaTiVCr high-entropy alloy and its derivative alloys for fusion material applications. Sci. Rep. **7**(1), 1926 (2017)
16. Karthik, S.; Prakash, K.S.; Gopal, P.M.; Jothi, S.: Influence of materials and machining parameters on WEDM of Al/$AlCoCrFeNiMo_{0.5}$ MMC. Mater. Manuf. Process. **34**(7), 759–768 (2019)
17. Mallick, A.; Vedantam, S.; Lu, L.: Grain size dependent tensile behavior of Mg–3% Al alloy at elevated temperatures. Mater. Sci. Eng. A **515**(1–2), 14–18 (2009)
18. Arab, A.; Guo, Y.; Zhou, Q.; Chen, P.: Fabrication of nanocrystalline AlCoCrFeNi high entropy alloy through shock consolidation and mechanical alloying. Entropy **21**(9), 880 (2019)
19. Veerappan, G.; Ravichandran, M.; Mohanavel, V.; Pritima, D.; Rajesh, S.: Effect of copper on mechanical properties and corrosion behavior of powder metallurgy processed Ni–Co–Cr–Fe–Mn–Cu_x high entropy alloy. Arab. J. Sci. Eng. **48**, 2905–2915 (2023)
20. Pradeep, N.B.; Hegde, M.R.; Patel, G.M.; Giasin, K.; Pimenov, D.Y.; Wojciechowski, S.: Synthesis and characterization of mechanically alloyed nanostructured ternary titanium based alloy for bio-medical applications. J. Market. Res. **16**, 88–101 (2022)
21. Sokkalingam, R.; Tarraste, M.; Surreddi, K.B.; Mikli, V.; Muthupandi, V.; Sivaprasad, K.; Prashanth, K.G.: Powder metallurgy of $Al_{0.1}$CoCrFeNi high-entropy alloy. J. Mater. Res. **35**(21), 2835–2847 (2020)
22. Zou, Y.; Wheeler, J.M.; Ma, H.; Okle, P.; Spolenak, R.: Nanocrystalline high-entropy alloys: a new paradigm in high-temperature strength and stability. Nano Lett. **17**(3), 1569–1574 (2017)
23. Rogal, Ł; Szklarz, Z.; Bobrowski, P.; Kalita, D.; Garzeł, G.; Tarasek, A.; Kot, M.; Szlezynger, M.: Microstructure and mechanical properties of Al–Co–Cr–Fe–Ni base high entropy alloys obtained using powder metallurgy. Met. Mater. Int. **25**, 930–945 (2019)
24. Oleszak, D.: Mechanical alloying-a novel method for synthesis and processing of materials. Acta Phys. Pol. A **96**(1), 101–112 (1999)
25. Chen, Z.W.; Sharp, R.M.; Gregory, J.T.: Fe–AI–Zn ternary phase diagram at 450 °C. Mater. Sci. Technol. **6**(12), 1173–1176 (1990)
26. Köster, M.; Schuhmacher, B.; Sommer, D.: The influence of the zinc content on the lattice constants and structure of the intermetallic compound Fe_2Al_5. Steel Res. **72**(9), 371–375 (2001)
27. Gedevanishvili, S.; Deevi, S.C.: Processing of iron aluminides by pressureless sintering through Fe+ Al elemental route. Mater. Sci. Eng. A **325**(1–2), 163–176 (2002)

28. Sina, H.; Corneliusson, J.; Turba, K.; Iyengar, S.: A study on the formation of iron aluminide (FeAl) from elemental powders. J. Alloy. Compd. **636**, 261–269 (2015)
29. German, R.M.: Transient thermal effects in the synthesis of intermetallic alloys. Therm. Anal. Metall. 205–32 (1992)
30. Xiong, C.; Ma, M.; Wu, C.: Explorations of stability, mechanical and thermal properties of cubic TiM2Al (M= Fe Co, Ni, and Cu) compounds. Solid State Commun. **340**, 114530 (2021)
31. Kumar, S.; Ghosh, S.K.: Porosity and tribological performance analysis on new developed metal matrix composite for brake pad materials. J. Manuf. Process. **59**, 186–204 (2020)
32. Gorban, V.F.; Zakiev, I.M.; Kurilenko, D.V.: Mechanical characteristics of high-entropy alloys and their constituent metals in friction conditions at low sliding velocities. Powder Metall. Met. Ceram. **58**, 265–269 (2019)